Journal of
Marine Science
and Engineering

Article

Study on the Relationship between Resistivity and the Physical Properties of Seafloor Sediments Based on the Deep Neural Learning Algorithm

Zhiwen Sun [1,2,3,4], Zhihan Fan [2,*], Chaoqi Zhu [2], Kai Li [2], Zhongqiang Sun [2], Xiaoshuai Song [2], Liang Xue [2], Hanlu Liu [2] and Yonggang Jia [2,*]

[1] Key Laboratory of Gas Hydrate, Ministry of Natural Resources, Qingdao Institute of Marine Geology, Qingdao 266237, China; zhiwensun91@163.com
[2] Shandong Key Laboratory of Marine Environmental Geology Engineering, Ocean University of China, Qingdao 266100, China
[3] Laboratory for Marine Mineral Resources, Pilot National Laboratory for Marine Science and Technology, Qingdao 266237, China
[4] Technology Innovation Center for Marine Methane Monitoring, Ministry of Natural Resources, Qingdao 266237, China
* Correspondence: fanzhihan@ouc.edu.cn (Z.F.); yonggang@ouc.edu.cn (Y.J.)

Abstract: The occurrence of deep-sea geohazards is accompanied by dynamic changes in the physical properties of seafloor sediments. Therefore, studying the physical properties is helpful for monitoring and early warnings of deep-sea geohazards. Existing physical property inversion methods have problems regarding the poor inversion accuracy and limited application scope. To address these issues, we establish a deep learning model between the resistivity of seafloor sediment and its density, water content, and porosity. Compared with empirical formulas, the deep learning model has the advantages of a more concentrated prediction range and a higher prediction accuracy. This algorithm was applied to invert the spatial distribution characteristics and temporal variation of the seafloor sediment density, water content, and porosity in the South China Sea hydrate test area for 12 days. The study reveals that the dynamic changes in the physical properties of seafloor sediments in the South China Sea hydrate zone exhibit obvious stratification characteristics. The dynamic changes in the physical properties of seafloor sediments are mainly observed at depths of 0–0.9 m below the seafloor, and the sediment properties remain stable at depths of 0.9–1.8 m below the seafloor. This study achieves the monitoring and early warning of dynamic changes in the physical properties of seafloor sediments and provides a guarantee for the safe construction of marine engineering.

Keywords: sediment resistivity; physical property; deep learning; the South China Sea

check for updates

Citation: Sun, Z.; Fan, Z.; Zhu, C.; Li, K.; Sun, Z.; Song, X.; Xue, L.; Liu, H.; Jia, Y. Study on the Relationship between Resistivity and the Physical Properties of Seafloor Sediments Based on the Deep Neural Learning Algorithm. *J. Mar. Sci. Eng.* **2023**, *11*, 937. https://doi.org/10.3390/jmse11050937

Academic Editor: George Kontakiotis

Received: 1 March 2023
Revised: 9 April 2023
Accepted: 12 April 2023
Published: 27 April 2023

1. Introduction

Seabed geohazards in the South China Sea [1], such as landslides [2,3], turbidity currents [4,5], and liquefaction [6], pose a significant risk to marine engineering projects [7], such as gas hydrate extraction [8,9], offshore oil and gas platform construction [10], and submarine fiber optic cables [11,12]. This is an urgent issue for national deep-sea development [13]. The process of incubation and the occurrence of deep seabed geohazards is characterized by dynamic changes in the engineering geological properties of sediments [14]. Current studies on engineering geological properties of submarine sediments and other related topics are mostly based on empirical formulas [15] with low prediction accuracy.

The method of neural networks was proposed in 1950 [16], but it was not until 2010 and GPU studies were improved that it became one of the most important methods of deep learning [17]. At present, artificial neural networks are widely used in studies of seabed sediments [18]. In 2006, Singh et al. [19] used artificial neural networks to predict aquifers in sediments by inverting vertical resistivity bathymetry data. Similarly, in 2009, Luo et al. [20] used the backpropagation (BP) artificial neural network in Matlab to study the physical properties of submarine sediments. The backpropagation artificial neural network was established with porosity, density, and water content as the input parameters and sound velocity as the output parameter. In 2016, Mukherjee et al. [21] developed an artificial neural network to predict the porosity and saturation of gas hydrates in reservoirs. The input parameter was density logs and the output parameters were porosity and saturation. In 2018, Zhou et al. [22] reviewed the application of deep learning algorithms based on the Keras database in Python language in the field of geology. In 2021, Singh et al. [23] employed neural networks to estimate gas hydrate saturation in sediments using porosity, bulk density, and P wave velocity as the input parameters. They compared 12 different machine learning algorithms and obtained a prediction accuracy of approximately 84%, which was higher than the accuracies of seismic and resistivity methods, which do not exceed 75%. In 2021, Chen employed an artificial neural network algorithm based on machine learning to invert acoustic impedance and CPT data [24]. In 2022, Singh et al. [25] used machine learning methods and nuclear magnetic resonance (NMR) data from downhole gas hydrate reservoirs to classify lithology. AI automation also has applications in mineralogy, and in 2022, Pszonka et al. applied SEM automation to mineral and texture sorting in gravity flows from seafloor sediments [26].

Most of the studies in this field have focused on using artificial intelligence methods to establish the relationship between the physical properties of seafloor sediments and geophysical parameters. However, the predicted values are mostly single discrete labels, and there is a lack of research on the dynamic changes in the physical properties of seafloor sediments. This study aims to construct a single-input, multiple-output deep neural learning algorithm for predicting the physical properties of seafloor sediments in the hydrate test area in the South China Sea.

2. Geological Background

2.1. Overview of the South China Sea Hydrate Test Area

The focus of this study is a hydrate test area located in the Shenhu Sea region of the South China Sea (Figure 1). The study area is situated within the Baiyun Depression, which forms part of the Pearl River Estuary Basin and is positioned between the Xisha Trough and Dongsha Islands [27] at a water depth of 1342 m. The geological setting of the study area is characterized by the interaction of several tectonic plates, including the Eurasian, Pacific, and Sino-Indian plates. The region exhibits both passive and active continental features, and displays a complex seafloor topography with varying elevations, characterized by the presence of erosion channels, sea valleys, seamounts, steep slopes, plateaus, alluvial fans, landslides, and other geological hazards. The dominant substrate in the study area is argillaceous silt.

2.2. Study Material of Core Sediments from the South China Sea

In 2020, we boarded the “Ocean Geology No. 6” research vessel of the Guangzhou Marine Geological Survey Bureau and obtained an 8 m long sediment core sample from the natural gas hydrate test area on the northern continental slope of the South China Sea. The engineering geological properties of the sediment, including density, water content, liquid limit, particle size composition, consolidation, cohesion, and internal friction angle, were obtained through laboratory geotechnical tests (Figure 2). The core sediment test results showed that the density of the seabed sediment in the South China Sea hydrate test area ranged from 1.32 to 1.50 g/cm^3, the water content ranged from 119% to 148%, the liquid limit ranged from 83.35 to 101.54, and the plastic limit ranged from 29.60 to 43.05. The range of the liquidity index was 0.90 to 1.95 and the range of plasticity index was 40.83 to 65.46. The sediment in the study area has the physical characteristics of a low density, a high water content, and a high compressibility [28].

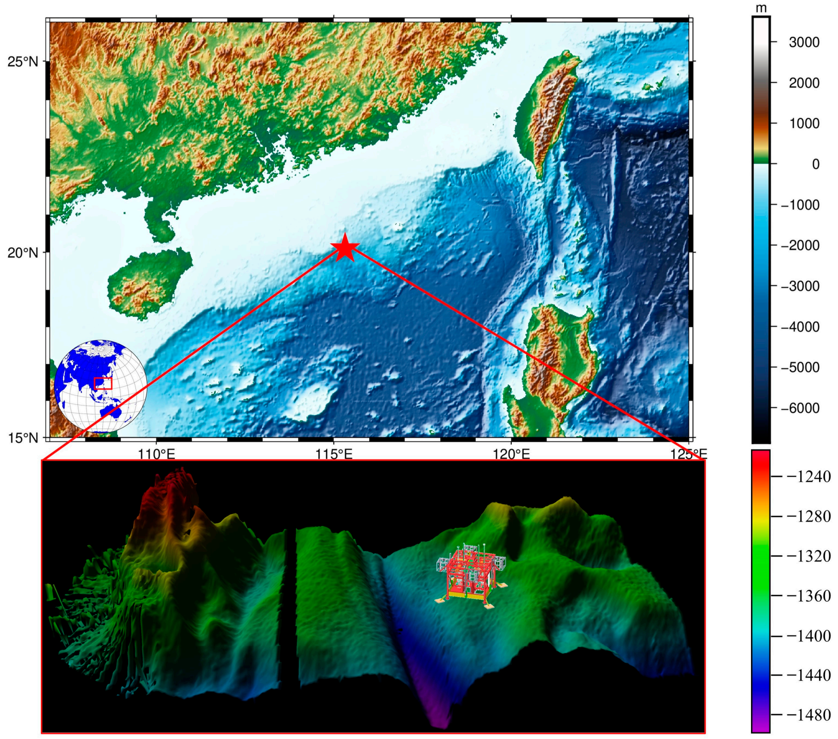

Figure 1. The study area for physical property inversion of seafloor sediments in the South China Sea hydrate test area.

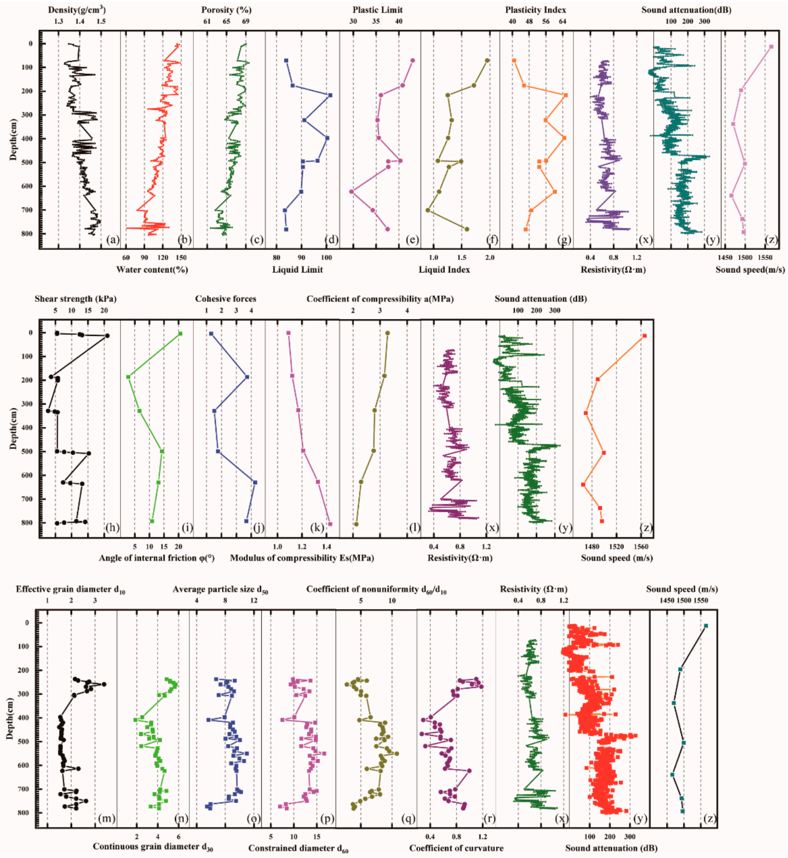

Figure 2. Physical and mechanical properties of sediments in the South China Sea (a, b, c, d, e, f, g, h, i, j, k, l, m, n, o, p, q, r, x, y, z are the sediment properties with depth, such as density, water content,

porosity, liquid limit, plastic limit, liquid index, plasticity index, shear strength, angle of internal friction, cohesive forces, modulus of compressibility, coefficient of compressibility, effective grain diameter, continuous grain diameter, average particle size, constrained diameter, coefficient of nonuniformity, coefficient of curvature, resistivity, sound attenuation, sound speed).

3. Deep Learning Inversion Method

3.1. Construction of Datasets

The present study utilizes a dataset consisting of multiple labels, including resistivity, density, water content, and porosity of sediments, for training and modeling. The training dataset was constructed using both actual measured data of seafloor sediments from the hydrate test area in the South China Sea, as well as the literature data collected from various locations such as the Yellow River estuary [29], offshore of Ningbo [30], and the northern land slope of the South China Sea [31]. The input parameter in the dataset is resistivity, while the output parameters are density, water content, and porosity.

3.1.1. Data Scatter Matrix

The scatter matrix visualization method is a highly effective tool for exploratory data analysis, typically using one feature as the x-axis and another feature as the y-axis. It facilitates the identification of relationships between features and enables the selection of optimal input and output parameters and the detection of outliers and other anomalies in the data [32]. The scatterplot matrix comprises two basic types of plots, namely a scatterplot and a histogram. The scatterplot above and below the diagonal presents the relationship between variables, while the histogram on the diagonal represents the variable distribution [33]. The scatterplot matrix of the actual measured data is presented in Figure 3.

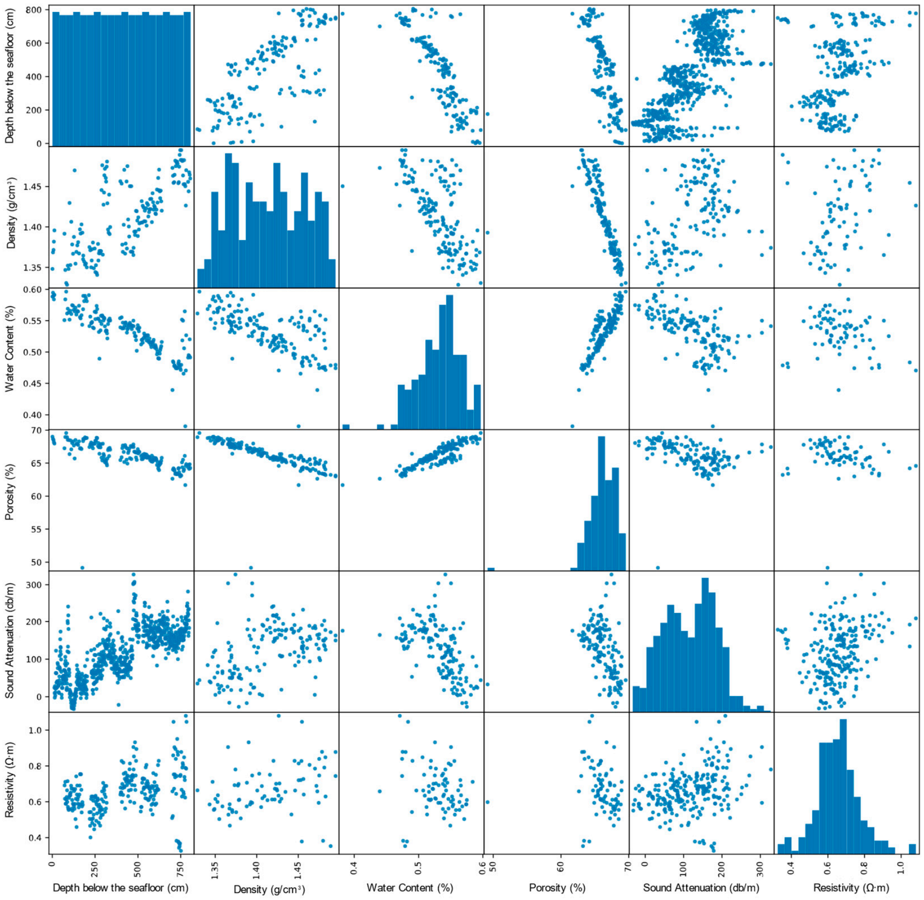

Figure 3. Data scatter matrix plot of burial depth below the seafloor, density, water content, porosity, sound attenuation, and resistivity of seafloor sediments in the South China Sea hydrate test area.

3.1.2. Data Preprocessing

Data with widely different value ranges can pose challenges for neural network learning, as the network may struggle to adapt to such variations. To address this issue, it is necessary to preprocess the input data by scaling each feature individually [34]. The most effective method is standardizing each feature, which entails subtracting the feature mean and dividing the result by the standard deviation for each feature of the input data (Equation (1)). This can result in data compression and distinctive data characteristics, namely a mean value of 0 and a standard deviation of 1 for each feature of the dataset.

$$z = \frac{x - \mu}{\sigma} \tag{1}$$

where x is the raw data, μ is the mean of the raw dataset, and σ is the standard deviation of the raw dataset.

3.1.3. Train–Test Dataset Split

The dataset in this study was partitioned into a training set and a test set, wherein the former comprises 75% of the data and the latter comprises 25%. To minimize the risk of errors due to arbitrary partitioning, the train_test_split() function was utilized for partitioning the dataset, with the random seed specified as RandomState = 0 to ensure the reproducibility of the results. Subsequently, the input and output parameters were separated for both the training and test sets.

3.2. Construction of the Deep Learning Model

This study presents a physical property prediction model for seafloor sediments in the hydrate test area of the South China Sea. The proposed model employs a nonlinear network topology and was developed using the functional APIs provided in the TensorFlow and Keras modules of Python. The functional API can directly manipulate the tensor, utilizing layers as functions that receive and return the tensor. This differs from the sequential model implementation of neural networks, which is limited to single-input and single-output models [35]. The functional API model is more general and flexible, allowing for the implementation of multiple input models, multiple output models, and graph-like models, and is therefore a suitable approach for addressing the problem at hand.

The neural network is comprised of layers, which function as data processing modules that convert input tensors into output tensors. The selection of layers depends on the tensor format and data processing requirements. In this study, a deep network learning model with seven layers was constructed, consisting of one input layer, one output layer, and five implicit neural network layers. The five implicit neural network layers contain four dense layers and one residual layer (Figure 4). The dense layer was used to train the neural network, while the last layer of the neural network was set as a one-unit linear layer without an activation function. The inclusion of an activation function would restrict the input range, limiting the prediction of density, water content, and porosity to within certain ranges. Additionally, a residual connection was incorporated into the model to prevent the loss of input resistivity information during data processing. The residual connection allows for the overlaying of the previous output tensor with the subsequent output tensor, ensuring the reinjection of previous resistivity information into the downstream data stream.

3.2.1. K-Fold Verification

When adjusting the parameters of a neural network, it is crucial to evaluate its performance. However, when the available data are scarce, a small validation set may result in significant fluctuations in the validation scores. Moreover, different ways of partitioning the validation set can further increase the variance of the validation scores, which hinders reliable model evaluation [36]. To address this issue, the K-fold cross-validation approach was employed in this study. The data in this paper were divided into five training and validation sets using the K-fold cross-validation method. Additionally, five identical models were built. Each model was trained on four partitions and evaluated on the remaining one. The validation score of the model was computed as the average of the five validation scores.

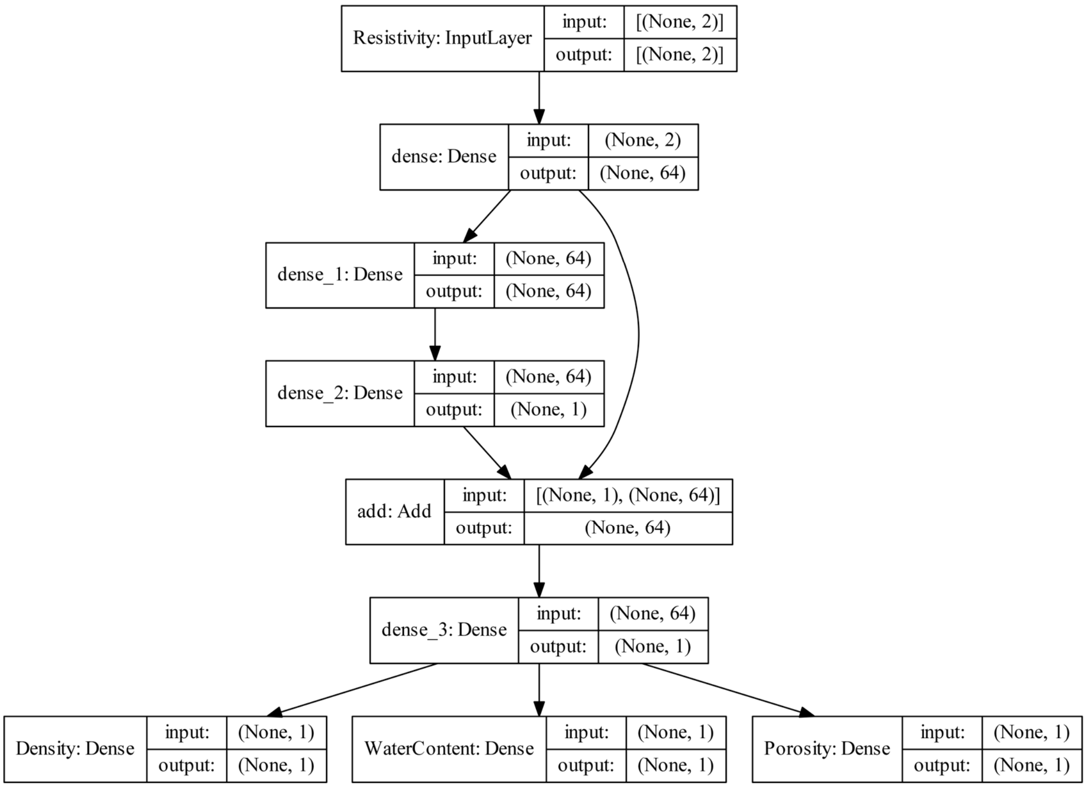

Figure 4. The framework of the deep learning neural network model based on resistivity inversion of seafloor sediment density, water content, and porosity.

3.2.2. Performance Evaluation Criteria

The loss function is one of the most important performance evaluation criteria and is used for the feedback signal of learning. The mean square error (MSE) loss function, which quantifies the squared difference between predicted and target values, was utilized in this prediction model (Equations (2) and (3)). In order to monitor the progress of the learning process, a new metric, the mean absolute error (MAE), was employed [37]. This metric measures the absolute value of the difference between the predicted and target values. By monitoring the MAE during the training process, the performance of the learning process can be evaluated and adjusted accordingly.

$$\mathrm{MSE} = \frac{1}{N}\sum_{t=1}^{N}(y_t - f_t)^2 \tag{2}$$

$$\mathrm{MSE} = \frac{1}{N}\sum_{t=1}^{N}\left|\frac{y_t - f_t}{y_t}\right| \tag{3}$$

3.3. Resistivity Observations of Seafloor Sediments in the South China Sea Hydrate Test Area

We have developed SEEGeo (In Situ Surveying Equipment of Engineering Geology in Complex Deep Sea) in order to realize the in situ long term observation of the engineering geological properties of seabed sediments. The SEEGeo (Figure 5) can simultaneously measure the resistivity, sound velocity, and excess pore pressure water pressure of the sediment [38]. Therefore, long-term observations of the resistivity of seafloor sediments were conducted in the hydrate test area of the South China Sea. The equipment was operated once a day, and a total of 12 days of data were collected from 15 to 27 September.

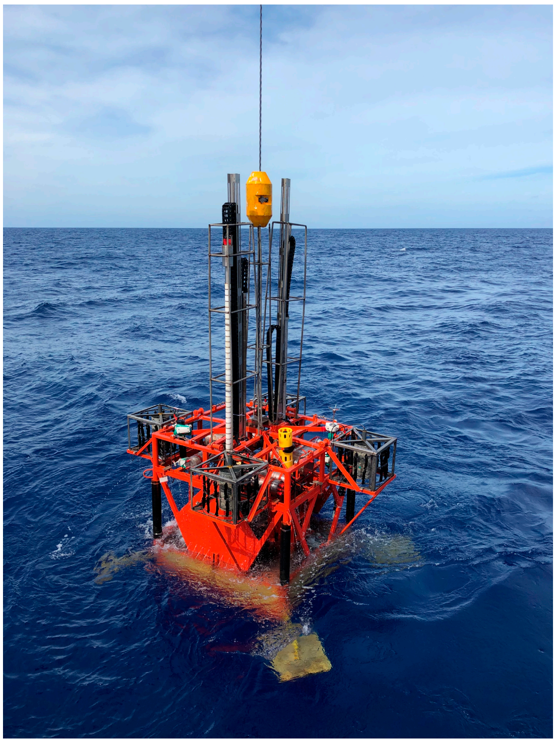

Figure 5. In Situ Surveying Equipment of Engineering Geology in Complex Deep Sea, SEEGeo.

4. Results and Discussion

4.1. Relationship between Sediment Resistivity and Physical Properties

4.1.1. Relationship between Sediment Resistivity and Density

Sediment density, which is the mass per unit volume of soil, displays considerable variability across diverse submarine sediments, and is closely linked to soil mineral composition, pore volume, and water content [39]. This study compares the relationship between resistivity and density derived from empirical equations, and the relationship derived from the deep learning model. We also explore the conditions and ranges of applicability of these distinct models.

The correlation based on empirical equations between resistivity and density is as follows: (1) the density increases monotonically with the increase in resistivity and (2) the seafloor sediment resistivity varies between 0.32 and 1.43 Ω·m, with a corresponding density range of 1.32~2.13 g/cm^3. By fitting the resistivity and density datasets of the seafloor sediment with the empirical equation, a quadratic polynomial relationship between these two variables can be derived (Equation (4)).

$$y = -0.31x^2 + 1.96x - 1.50 \tag{4}$$

The result indicates that the correlation between seafloor sediment resistivity and density based on the empirical equation is poor, with an R^2 value of 0.33. The traditional empirical formula is inadequate as a fitting model for the resistivity–density correlation.

We explored the correlation between sediment resistivity and density based on deep learning (Figure 6). The results indicate that the relationship between these two properties follows a three-step trend: decreasing, increasing, and sharply increasing. More specifically, when the resistivity ranges from 0.32 to 0.46 Ω·m, the sediment density decreases as the resistivity increases, with a slope of −0.79 from 1.48 g/cm^3 to 1.37 g/cm^3. When the resistivity ranges from 0.46 to 1.15 Ω·m, the sediment density increases as the resistivity increases, with a slope of 0.25 from 1.37 g/cm^3 to 1.54 g/cm^3. Finally, when the resistivity is between 1.15 and 1.43 Ω·m, the sediment density increases sharply as the resistivity increases, with a slope of 1.04 from 1.54 g/cm^3 to 1.83 g/cm^3. These findings suggest that the deep learning model can reveal complex relationships between sediment properties, which may not be captured by traditional empirical formulas.

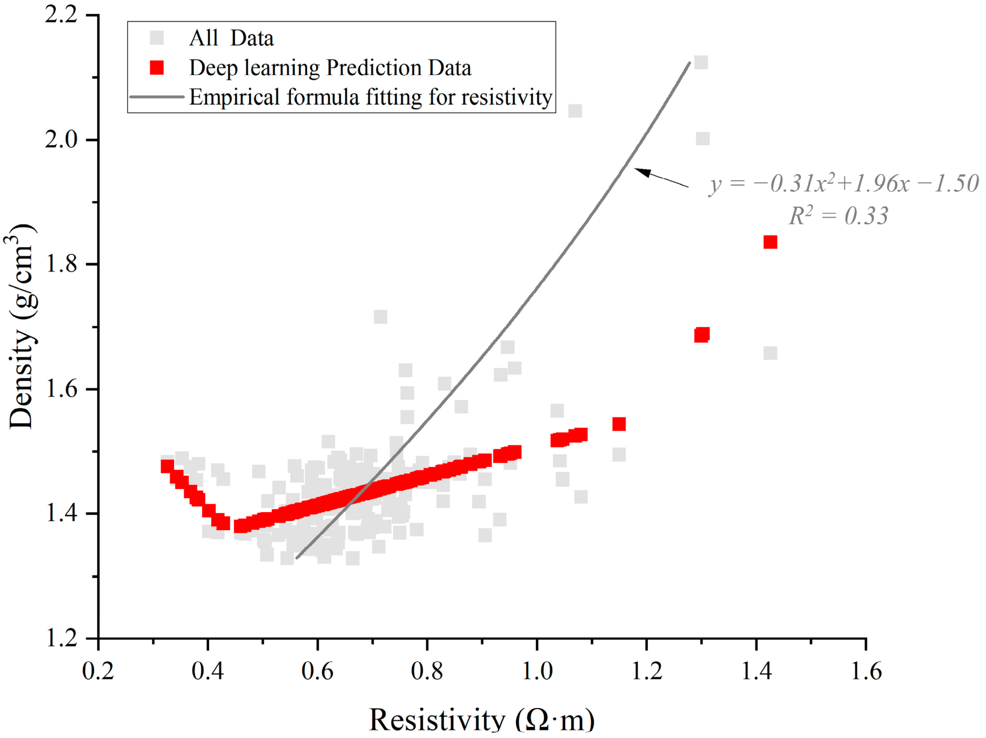

Figure 6. Correlation between sediment resistivity and density based on empirical equation and deep learning model (data source: measured data from the South China Sea and reference data of the Yellow River estuary sediment [29], Ningbo offshore sediment [30], the South China Sea [31]).

The present study investigated the relationship between sediment resistivity and density using both empirical and deep learning models. The results indicate that: (1) The deep learning model predicts that the sediment resistivity is not monotonically related to density, indicating that the same sediment density may have different resistivity values. (2) The resistivity cannot be solely determined based on density in the range of 1.38 to 1.47 g/cm^3 and the range of 0.33 to 0.83 Ω·m, as there are multiple solutions, but can be determined based on density when the density exceeds 1.47 g/cm^3. (3) The sediment density can be uniquely determined based on resistivity. (4) The sediment density is more sensitive to changes in resistivity when the resistivity is >1.15 Ω·m, where changes in density per unit of resistivity correspond to larger values. (5) The correlation coefficient between resistivity and density based on the empirical equation is very low, with a value of 0.33. The R^2 correlation coefficient is typically used in linear models and may not fully capture the predictive ability of the model in nonlinear models. Moreover, the correlation coefficient is closely related to the sample size of the dataset, and the model results can vary widely across different datasets.

4.1.2. Relationship between Sediment Resistivity and Water Content

Seafloor sediments are typically saturated or nearly saturated, with water content playing a crucial role in the design of seafloor engineering structures [40]. An increase in water content results in an improved fluid connectivity of sediment pores, leading to an enhanced electrical conductivity and, correspondingly, a lower resistivity. In contrast, sediments with a low water content exhibit a higher resistivity, and water with various ions functions as a good electrical conductor [30]. Despite a decline in resistivity with the decreasing water content in the saturated state, the magnitude of change diminishes [31]. The primary factors influencing sediment resistivity in descending order are water content, pore water conductivity, soil saturation, and soil type [41].

The present study investigated the correlation between sediment resistivity and the water content of seafloor sediment based on an empirical formula. The resistivity of the seafloor sediment varied between 0.32 and 2.17 Ω·m, while the water content ranged from 24% to 154%. By fitting the relationship between the resistivity and the water content of the seafloor sediment with the empirical equation, a power function relationship (Equation (5)) between these two variables can be derived.

$$y = 52.83x^{-1.745} \tag{5}$$

The results indicated a power function relationship between the resistivity and the water content of the seafloor sediment. In particular, the resistivity decreased sharply at first with the increase in water content, followed by a slow decrease. These findings suggest that water content plays an important role in determining the resistivity of the seafloor sediment and should be taken into consideration when modeling the resistivity. However, we need to develop more accurate models for predicting the sediment resistivity based on water content.

The deep learning model reveals a correlation between sediment resistivity and water content characterized by a three-step trend (Figure 7). Specifically, the water content exhibits a slow and linear decrease with increasing resistivity, followed by a rapid decrease expressed by a power function, and a subsequent slow and linear decrease. This trend is observed in three distinct resistivity ranges. For resistivities between 0.33 and 0.72 Ω·m, the water content decreases slowly and linearly with increasing resistivity, with a slope of -12.82, resulting in a decrease from 120% to 115%. For resistivities ranging from 0.72 to 1.16 Ω·m, the water content rapidly decreases with increasing resistivity in a power function with a negative exponent, with a slope of -12.82, resulting in a decrease from 115% to 115%. Finally, for resistivities between 1.16 and 2.17 Ω·m, the water content decreases slowly and linearly with increasing resistivity, with a slope of -24.75, resulting in a decrease from 41% to 16%.

The present study investigated the relationship between water content and resistivity using both empirical and deep learning models. The results indicate that: (1) The deep learning model shows a monotonically decreasing relationship between water content and resistivity, which is one-to-one and without multi-solution. (2) The correlation between water content and resistivity is characterized by both a linear decreasing function and a negative exponential power function in the deep learning model. For sediment resistivity values of <0.71 Ω·m (i.e., water content > 115%), a linear decreasing function of water content to resistivity is observed. The prediction result of the empirical formula model is an exponential function and differs significantly from the deep learning prediction model. For sediment resistivity values between 0.71 and 1.33 Ω·m (i.e., a water content between 34 and 115%), the prediction results of the empirical formula model are in good agreement with those of the deep-learning-based prediction model. For sediment resistivity values of >0.71 Ω·m (i.e., a water content < 115%), the deep learning prediction model fits better than the empirical formula. (3) The sensitivity of water content to resistivity is higher for resistivity values of >0.71 Ω·m (i.e., a water content < 115%), implying that a unit change in resistivity corresponds to a larger change in water content. Therefore, the inversion of water content in this interval is more accurate.

4.1.3. Relationship between Sediment Resistivity and Porosity

The sediment porosity is a critical physical parameter that characterizes the total volume of pores within the sediment. The influence of sediment porosity on the resistivity magnitude is significant. Sediments with a higher porosity possess a larger pore space that facilitates better connectivity within the pore network. As a result, the fluid within the pore has a higher mobility, leading to improved electrical conductivity and lower resistivity [42].

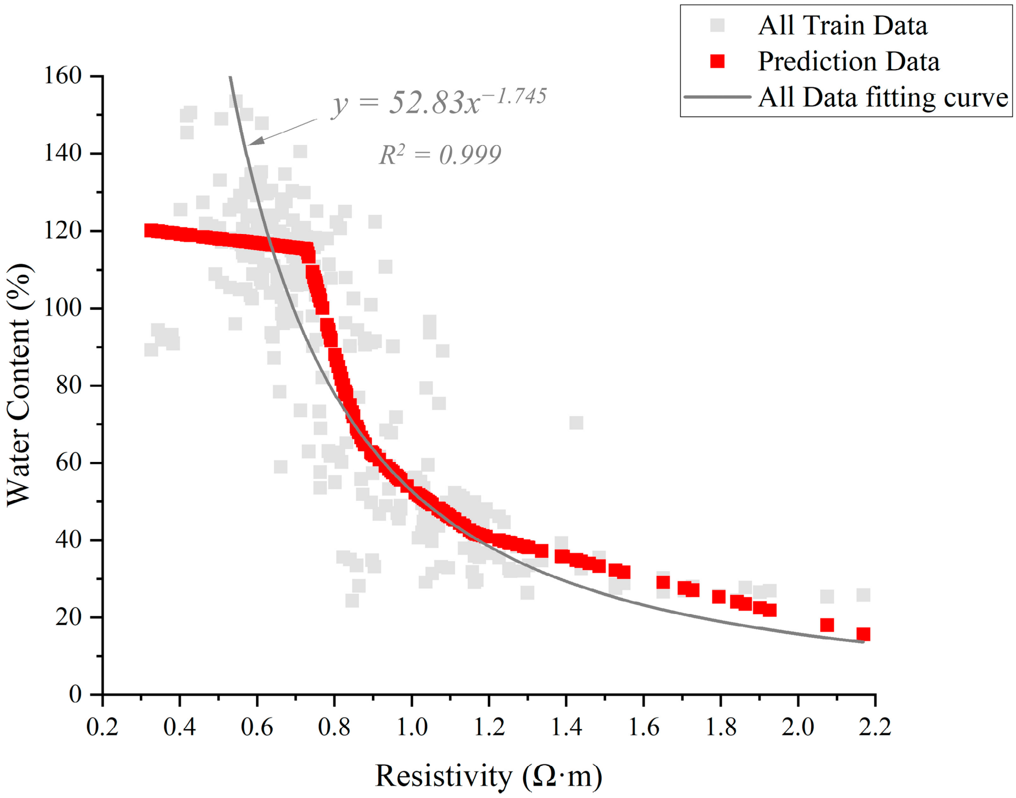

Figure 7. Correlation between sediment resistivity and water content based on an empirical equation and the deep learning model (data source: measured data from the South China Sea and reference data of the Yellow River estuary sediment [29], Ningbo offshore sediment [30], the South China Sea [31]).

The empirical equations reveal a correlation between sediment resistivity and porosity, where the seafloor sediment resistivity ranges between 0.32 and 1.93 Ω·m, while the porosity of the sediment ranges from 36.81 to 79.52%. The seafloor surface sediment exhibits a strong linear relationship between sediment resistivity and porosity (Equation (6)).

$$y = -26.58x + 84.08 \tag{6}$$

The present study demonstrates a favorable correlation between the resistivity and the porosity of seafloor sediments based on empirical formulas with an R^2 value of 0.97, indicating a high degree of correlation. The traditional empirical formulas exhibit good fits to the data, although discrepancies are observed in the predicted values at both low and high resistivity ranges.

This study employed deep learning to investigate the correlation between sediment resistivity and porosity (Figure 8). The results reveal that the porosity of seafloor sediments follows a three-step trend with increasing resistivity, characterized by extremely slow, slow, and rapid decreases. Specifically, for resistivities of <0.50 Ω·m (i.e., 0.33–0.50 Ω·m), the sediment porosity decreases extremely slowly from 69.37% to 69.13%, with a slope of −1.41. In the range of 0.50–0.70 Ω·m, the sediment porosity decreases slowly from 69.13% to 66.74%, with a slope of −11.95. Finally, when the resistivity is greater than 0.70 Ω·m (i.e., 0.70 to 1.93 Ω·m), the sediment porosity decreases rapidly and linearly from 66.74% to 29.19% with a slope of −30.53. These findings provide a valuable contribution to the understanding of the intricate relationship between sediment resistivity and porosity, and can facilitate the enhancement in the accuracy of seafloor sediment characterization.

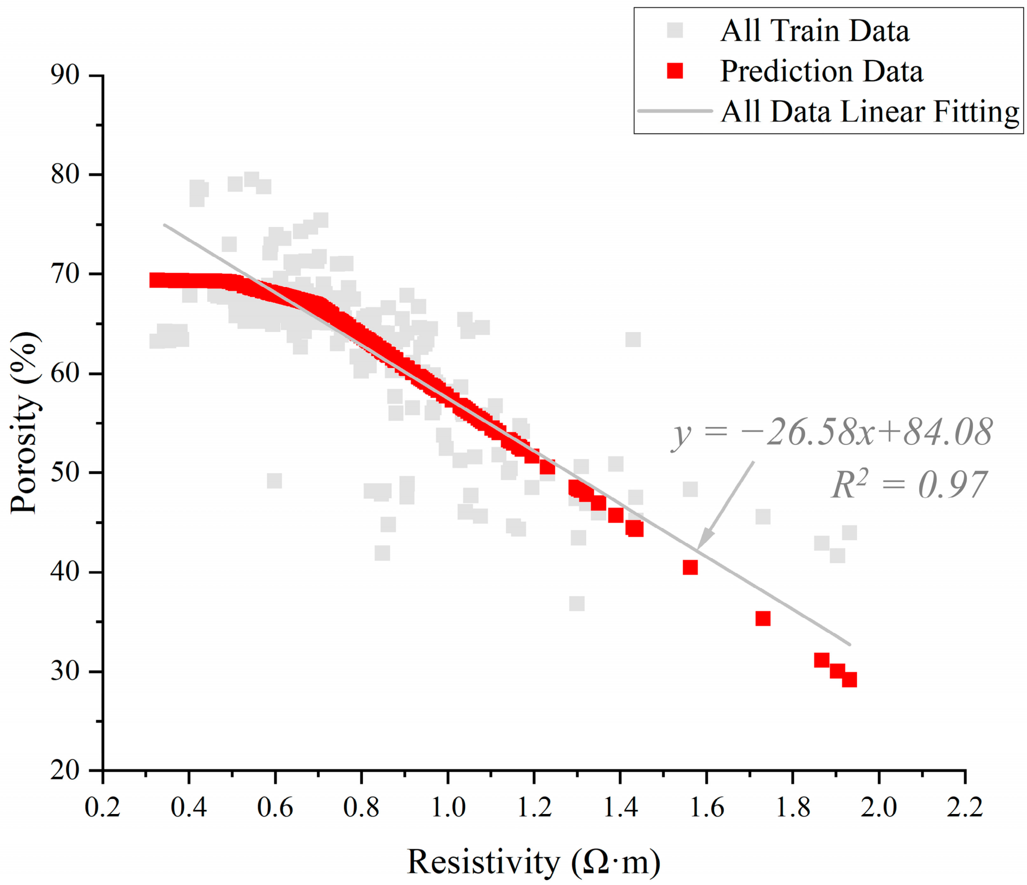

Figure 8. Correlation between sediment resistivity and porosity based on the empirical equation and the deep learning model (data source: measured data from the South China Sea and reference data of the Yellow River estuary sediment [29], Ningbo offshore sediment [30], the South China Sea [31]).

The present study investigated the relationship between sediment resistivity and porosity using both empirical and deep learning models. The results reveal that the sediment porosity and resistivity exhibit a monotonically decreasing function, indicating a one-to-one correspondence with no multi-solution. The deep learning model can be divided into three linearly decreasing functions, with the corresponding cutoff points of 0.5 Ω·m and 69.13% water content and 0.7 Ω·m and 66.74% water content. When the sediment resistivity is greater than 0.70 Ω·m, the sediment porosity is more sensitive to resistivity, and it is more accurate to invert the sediment density change by resistivity. Furthermore, when the sediment resistivity is less than 0.70 Ω·m and the water content is greater than 68%, the prediction values of the empirical formula model and the deep learning prediction model differ significantly, with the latter tending towards a constant value that is closer to the actual value. As the sediment porosity increases, the sediment resistivity approaches the seawater resistivity and exhibits a constant value. The correlation coefficient increases significantly with an increase in data samples, highlighting the superior performance of the deep learning model in describing the correlation between sediment resistivity and porosity compared to traditional models.

As a result, the deep neural network learning model exhibits superior performance and provides a more accurate prediction range compared to the empirical formula. The empirical formula inversion model is effective in analyzing linear relationships with simple correlations and high coefficients of determination. In contrast, the deep learning inversion model is suitable for examining nonlinear relationships with complex correlations and poor coefficients of determination. When training data are abundant, the deep learning inversion model outperforms the empirical formula model in terms of prediction accuracy. Specifically, the deep learning inversion model improves the accuracy of the prediction area by 50%, enhances the concentration of the prediction area, and increases the goodness-of-fit by 33%, thereby achieving a higher prediction accuracy.

4.2. In Situ Resistivity Observation Results in the South China Sea Hydrate Test Area

4.2.1. Spatial Structure of Seafloor Sediment Resistivity

The present study investigated the spatial structure of sediment resistivity within 1.80 m of the seafloor in the South China Sea hydrate test area (Figure 9). The resistivity of the seawater on 15 September was found to be 0.06 Ω·m, while the resistivity of the seafloor sediment ranged from 0.01 to 6.86 Ω·m, with a mean resistivity of 0.84 Ω·m and a median resistivity of 0.23 Ω·m. Most of the resistivity values were distributed between 0.01 and 2 Ω·m, with two extreme points at 0.9–1.1 m, 5.82, and 6.86 Ω·m, respectively. When focusing on the range of 0–2 Ω·m, most of the resistivity values were distributed between 0.01 and 1 Ω·m.

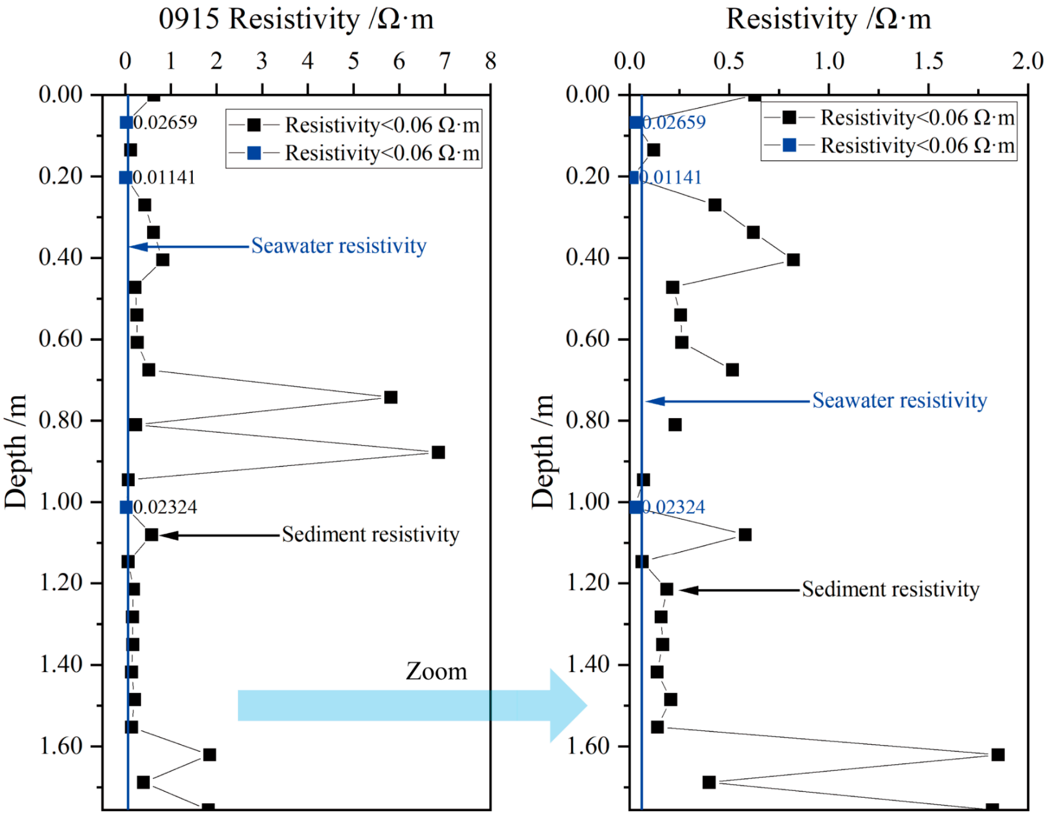

Figure 9. Spatial structure of sediment resistivity in the South China Sea (using 15 September as an example).

In this study, the first layer of sediment in the South China Sea hydrate test area was found to exhibit a low resistivity when buried at a depth of 0–0.07 m. The resistivity ranged from 0.01 to 0.83 Ω·m, with a variation rate of 0–71%. A total of 11 measurements were recorded in this layer, two of which exhibited resistivity values lower than that of seawater. Specifically, resistivity values of 0.03 Ω·m at a depth of 0.07 m and 0.01 Ω·m at a depth of 0.20 m were recorded.

The second layer of sediment was identified as a very high resistivity layer buried at depths ranging from 0.68 to 0.95 m. The resistivity of this layer varies from 0.07 to 6.86 Ω·m, exhibiting a variation rate of 5–600%. Within this layer, there were five measurement points, two of which had resistivity values significantly higher than the resistivity of the seafloor sediment (0.06–2 Ω·m). Specifically, the resistivity at a depth of 0.74 m was 5.82 Ω·m, which is 509% higher than the lowest value, and the resistivity at a depth of 0.88 m was 6.86 Ω·m, which is 600% higher than the lowest value.

The third layer of sediment was identified as a low resistivity layer, with a sediment depth ranging from 0.945 m to 1.5525 m. The resistivity values in this layer exhibit variations ranging from 0.02 Ω·m to 0.58 Ω·m, representing a variation rate of 1% to 59%. A total of 10 measurements were recorded within this layer, and it is noteworthy that one of these points situated at a depth of 1.01 m had a resistivity value of 0.02 Ω·m.

The fourth layer comprises high resistivity sediment buried at depths ranging from 1.55 to 1.76 m. The resistivity of the sediment varies from 0.14 to 1.85 Ω·m, with a variation rate of 11 to 161%. Four measurements were taken in this layer, out of which two had significantly higher resistivity values. At a depth of 1.62 m, the resistivity value was 1.85 Ω·m, indicating a variation rate of 161%. Similarly, at a depth of 1.76 m, the resistivity value was 1.82 Ω·m, indicating a variation rate of 159%.

4.2.2. The Variation in Seafloor Sediment Resistivity with Time

The present study investigated the dynamic changes i the resistivity of the seafloor sediment in the hydrate test area of the South China Sea over 12 days, from 15 to 27 September. The resistivity values of the seafloor sediment in the South China Sea hydrate test area ranged from 0.002 to 6.86 Ω·m, and were classified into three layers (Figure 10). The first layer, with resistivity values lower than the resistivity of seawater (<0.06 Ω·m), is shown in white. The second layer corresponds to the resistivity values of normal sediment (0.06–2 Ω·m) and is filled in blue. The third layer has resistivity values greater than the resistivity of normal sediment (>2 Ω·m) and is filled in green and red.

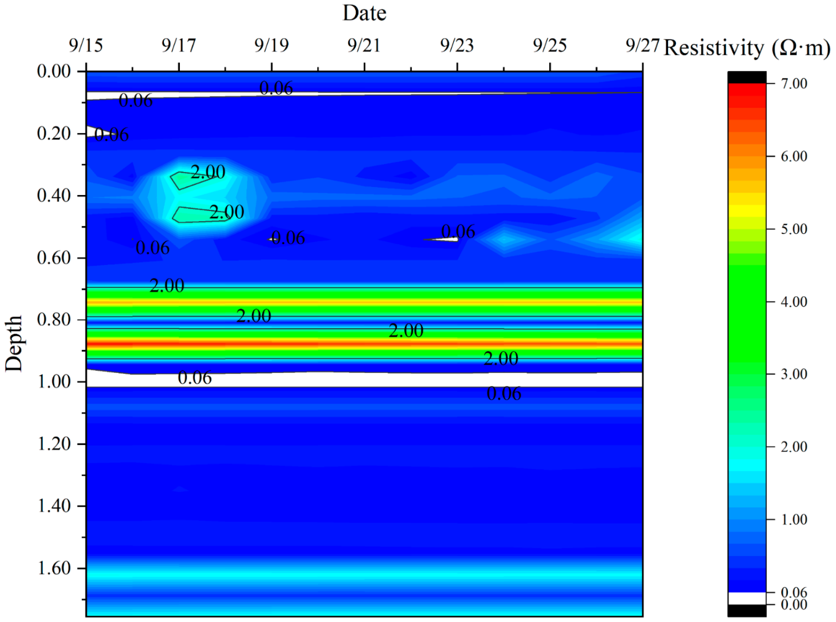

Figure 10. Time-varying curve of seafloor sediment resistivity in the South China Sea hydrate test area.

In the range of 0–1.755 m, the resistivity is divided into seven layers in the longitudinal structure, which are classified as a low resistivity layer, an ultra-low resistivity layer, a high resistivity layer, an ultra-high resistivity layer, an ultra-low resistivity layer, a low resistivity layer, and a high resistivity layer.

In the first layer, sediments are buried at a depth of 0–0.6 m in the normal low resistivity zone, and the resistivity variation ranges from 0.43 to 3.55 Ω·m. The resistivity does not change significantly over time.

The second layer, located at a sediment burial depth of 0.06~0.20 m, is characterized by ultra-low resistivity. Within this layer, there exist two distinct low resistivity zones, located at 0.06 and 0.20 m, respectively, with resistivity varying between 0.01 and 0.17 Ω·m. At a depth of 0.06 m, the resistivity gradually increases over time, ranging from 0.02 Ω·m to 0.06 Ω·m, ultimately approaching the resistivity value of seawater. Similarly, at a depth of 0.20 m, the resistivity also gradually increases over time, ranging from 0.01 Ω·m to 0.17 Ω·m, and reaches 0.08 Ω·m on the following day, 16 September, which is also close to the resistivity of seawater.

The third layer of sediment, with a burial depth of 0.33–0.47 m, is characterized by high resistivity. The resistivity in this layer ranges from 0.09 to 2.44 Ω·m and exhibits an increasing-then-decreasing trend. At a depth of 0.33 m, the resistivity increases from 0.62 Ω·m to 2.44 Ω·m and then decreases to 0.52 Ω·m. Similarly, at 0.40 m and 0.47 m, the resistivity increases and then decreases, with values changing from 0.82 Ω·m to 1.73 Ω·m to 0.64 Ω·m and from 0.21 Ω·m to 2.32 Ω·m to 1.22 Ω·m, respectively.

The fourth layer of sediment located at a depth of 0.67 to 0.94 m is characterized by ultra-high resistivity, which exceeds the normal sediment resistivity (>2 Ω·m). The resistivity ranges from 0.18 to 6.85 Ω·m, demonstrating a three-layer structure of high resistivity–low resistivity–high resistivity. The ultra-high resistivity layer at 0.74 m exhibits a gradual decrease in resistivity over time, from 5.82 Ω·m to 5.65 Ω·m. Likewise, the low resistivity layer at 0.81 m shows a decrease in resistivity with time, changing from 0.22 Ω·m to 0.18 Ω·m. In the ultra-high resistivity zone at 0.87 m, the resistivity gradually decreases with time from 6.85 Ω·m to 6.35 Ω·m.

The fifth layer of the sediment, a burial depth of 1.01 m, is an ultra-low resistivity zone with a resistivity even lower than that of seawater. The resistivity varies in a narrow range of 0.02~0.03 Ω·m and shows a trend of increasing initially and then decreasing, reaching a peak value of 0.03 Ω·m from 0.02 Ω·m before decreasing back to 0.02 Ω·m.

The fifth layer of the sediment, located at a burial depth of 1.08 to 1.55 m, exhibits a low resistivity. The resistivity values range between 0.06 and 0.58 Ω·m, and display little temporal variation, remaining in a stable state.

The seventh layer of sediment, located at a burial depth of 1.62–1.80 m, exhibits a high resistivity with a resistivity range of 0.38–1.88 Ω·m. At a depth of 1.62 m, the resistivity value is classified as a high resistivity and displays a gradually decreasing trend, declining from 1.85 Ω·m to 1.79 Ω·m. At 1.68 m, the resistivity is categorized as a low resistivity and exhibits little variation over time, with resistivity values oscillating between 0.38 and 0.40 Ω·m. The resistivity at a depth of 1.80 m is classified as a high resistivity and demonstrates a gradual increase from 1.82 Ω·m to 1.88 Ω·m.

The in situ observation structure of natural gas hydrates deposited on the seafloor exhibits a bimodal structure in resistivity. Jana et al. [43] pointed out that in the hydrate occurrence zone, the bimodal feature of the resistivity of the sediment layer indicates the presence of the hydrate layer. This paper presents resistivity observations of seafloor sediment in the South China Sea hydrate test area, which indicate that the resistivity at 0.7~0.9 m below the seafloor surface has a bimodal structure with a resistivity value of 7.0, indicating the presence of a thin layer of natural gas hydrate. The resistivity of the ultra-high resistivity layer at 0.74 m decreases gradually with time from 5.82 Ω·m to 5.65 Ω·m, while the resistivity of the low resistivity layer at 0.81 m decreases gradually from 0.23 Ω·m to 0.19 Ω·m over time. Similarly, the resistivity of the ultra-high resistivity zone at 0.88 m gradually decreases over time from 6.86 Ω·m to 6.35 Ω·m. The bimodal resistivity of the seafloor sediment is a typical characteristic of hydrate storage. Previous studies by Wu and Guo have also reported the bimodal structure of hydrate resistivity in seafloor sediments [44], with a resistivity value of approximately 7 Ω·m, consistent with the findings of this study.

4.3. Dynamic Changes in Physical Properties of Seafloor Sediments Based on Deep Learning Inversion

4.3.1. Temporal Variation in Seafloor Sediment Density in the South China Sea Hydrate Zone

The findings of the sediment density inversion of the seafloor in the South China Sea hydrate test area reveal distinct variations in sediment density at varying depths. The sediment within 0.7 m of the seafloor surface exhibited marked dynamic changes in density, whereas the density of sediment situated below 0.7 m remained essentially constant (Figure 11).

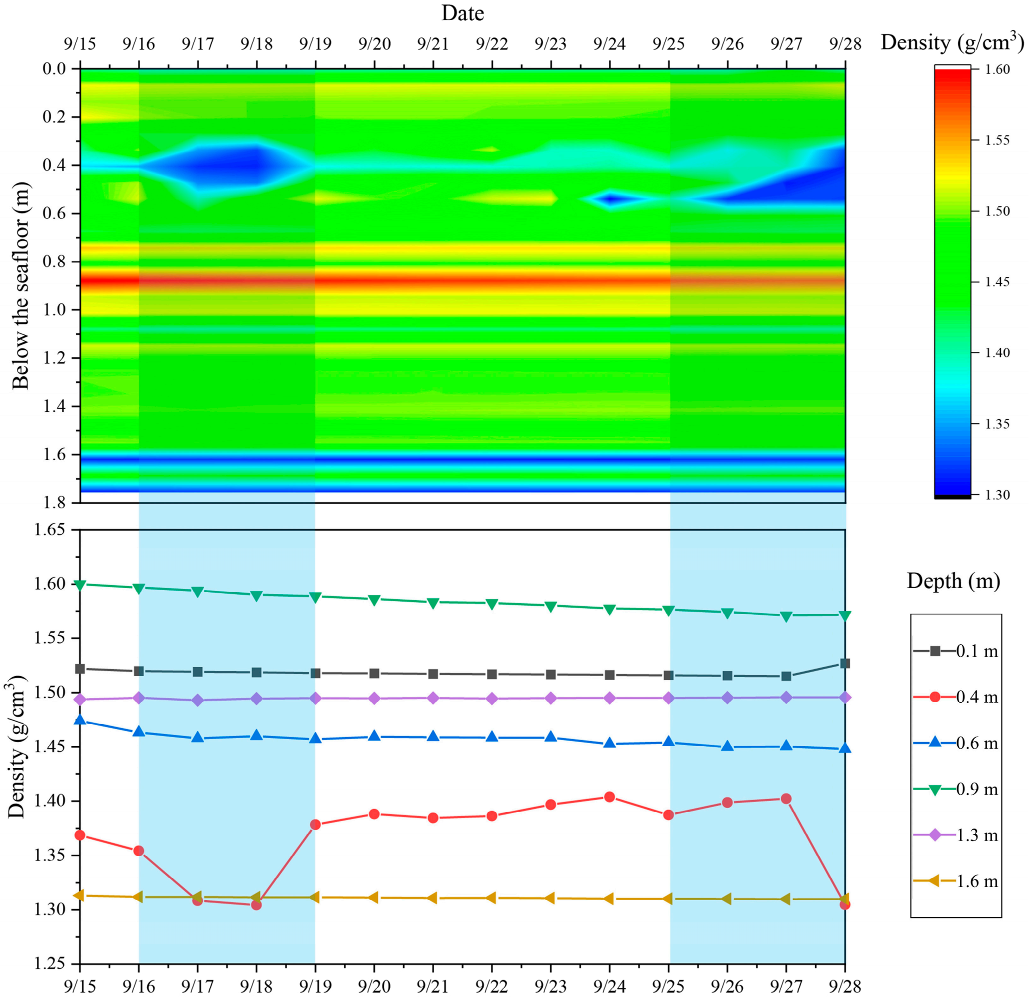

Figure 11. Temporal variation in density of the seafloor sediment in the South China Sea hydrate test area.

The present study depicts the temporal variation of sediment density, obtained through resistivity inversion of seafloor sediment in the South China Sea hydrate test mining area at a depth of 1.755 m below the seafloor surface. The sediment density exhibits a variation range of 1.30–1.60 g/cm^3, with distinct variation patterns observed among different sediment layers (Figure 11). Specifically, sediment samples collected from depths of 0.1, 0.4, 0.6, 0.9, 1.3, and 1.6 m below the seafloor surface were selected for analysis, and their density variation patterns were evaluated over time.

The results revealed varying patterns in sediment density with time at different depths. At a depth of 0.1 m, the sediment density fluctuated between 1.51 and 1.53 g/cm^3. Specifically, the density decreased gradually from 15 to 27 September, but then suddenly increased from 17 to 28 September. Within the depth range of 0.4 m, the sediment density varied between 1.30 and 1.40 g/cm^3. From 15 to 17 September, the density exhibited a rapid decrease, followed by a period of stability and no change until 27 September, when it suddenly decreased again. Within the depth range of 0.6 m, sediment density varied from 1.44 to 1.47 g/cm^3 and exhibited a gradual decrease from 15 to 28 September. At a depth of 0.9 m, the sediment density varied from 1.57 to 1.60 g/cm^3, representing a 2% decrease in density over time from 15 to 28 September. At the depth range of 1.3 m, the sediment density ranged from 1.49 to 1.50 g/cm^3, with a slow increase in density observed over the same time. At a depth of 1.6 m, the sediment density varied between 1.30 and 1.31 g/cm^3 and remained stable from 15 to 28 September.

At the depths of 0.1, 1.3, and 1.6 m below the seafloor surface, the sediment densities remained stable and unchanged, indicating that the sediment properties of these layers did not change during the measurement period. At the depth of 0.4 m below the seafloor surface, the sediment density exhibited a trend of "decrease–increase–decrease" with time. With increasing time, the sediment density of the sediment layer at a 0.4 m burial depth decreased, but the density of adjacent layers did not significantly change. It is assumed that there was no vertical transport of the sediment and that horizontal transport along the sediment layer may have occurred. A potential mechanism may be that when the horizontal fluid is transported, the fine sediment particles are transported and carried away first [45], leading to a reduction in sediment density. These observations suggest the possibility of fluid exchange between the soil and seawater at the site. The lack of changes in overlying sediment characteristics suggests that fluid transport occurs horizontally [46,47].

4.3.2. Temporal Dynamics of the Water Content in Seafloor Sediments in the South China Sea Hydrate Zone

The findings of the sediment water content inversion of the seafloor in the South China Sea hydrate test area reveal distinct variations in the sediment water content at varying depths. Specifically, the water content within 0.7 m below the seafloor showed pronounced dynamic changes, while the water content below 0.7 m remained relatively constant.

The present study investigated the temporal variations in water content in the seafloor sediment of the South China Sea hydrate test area at a depth of 1,755 m below the seafloor (Figure 12). The water content exhibited variations within the range of 42–125%, and different sediment layers displayed diverse patterns of variation. Specifically, the water content at depths of 0.1, 0.4, 0.6, 0.9, 1.3, and 1.6 m below the seafloor were selected for analysis to determine the time-dependent variation patterns.

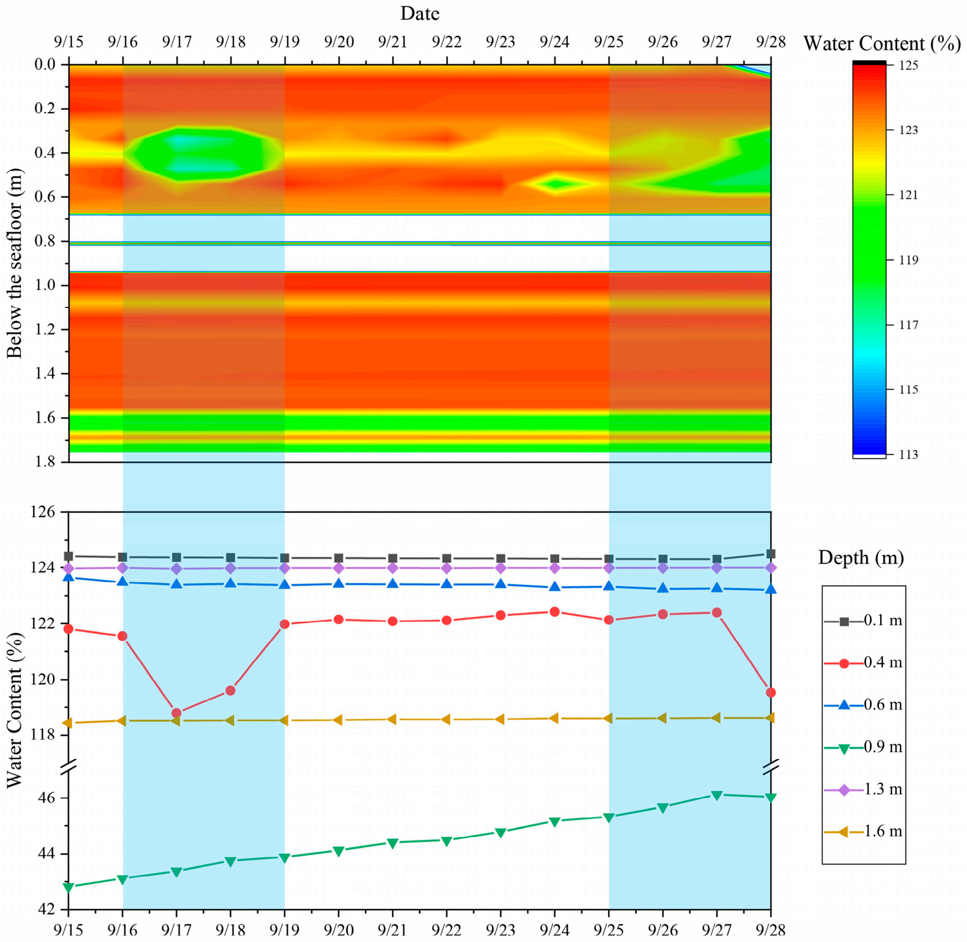

Figure 12. Temporal variation in water content of the seafloor sediment in the South China Sea hydrate test area.

In the South China Sea hydrate test area, the water content within specific depth intervals exhibited temporal variability. Within the depth interval of 0.1 m below the seafloor, the water content ranged between 124.3% and 124.5%. The water content gradually decreased from 15 to 27 September, with a sudden increase occurring between 17 and 28 September. Near the depth interval of 0.4 m below the seafloor surface, the water content ranged from 119.5% to 122.4%. Between 15 and 17 September, the water content decreased rapidly, followed by a stable and unchanged state between 17 and 27 September, and then a sudden decrease on 28 September. At the depth interval of 0.6 m below the seafloor surface, the water content ranged from 123.2% to 123.6%, gradually decreasing from 15 to 28 September. For the depth interval of 0.9 m below the seafloor surface, the water content ranged from 42.8% to 46.1%, exhibiting a 7% increase. Between 15 and 27 September, the water content gradually increased, followed by a slight decrease between 27 and 28 September. At the depth interval of 1.3 m below the seafloor surface, the water content ranged from 123.9% to 124.0%, remaining relatively stable from 15 to 28 September. Finally, for the depth interval of 1.6 m below the seafloor surface, the water content ranged from 118.4% to 118.6%, exhibiting little temporal variability over the same period.

In the water content study, stable sediment properties were found at the depths of 0.1, 1.3, and 1.6 m below the seafloor, as evidenced by the unchanging sediment porosity. However, at a depth of 0.4 m below the seafloor surface, the water content exhibited a temporal trend of "decrease–increase–decrease."

4.3.3. Temporal Dynamics of the Seafloor Sediment Porosity in the South China Sea Hydrate Test Area

The study of sediment porosity in the seafloor of the South China Sea hydrate test area using deep learning inversion techniques revealed varying patterns of variation at different depths (Figure 13). Specifically, the porosity of sediment below 0.7 m remained stable, whereas dynamic changes in the sediment porosity within 0.7 m of the seafloor surface are evident. These findings highlight the non-uniform distribution of sediment properties in the study area.

The temporal variation in the sediment porosity in the South China Sea hydrate test area was within the depth of 0~1.755 m below the seafloor. The sediment porosity varied within the range of 52~76%, and distinct layers of sediment porosity exhibited diverse variation patterns. The depths of 0.1, 0.4, 0.6, 0.9, 1.3, and 1.6 m below the seafloor were scrutinized to explore the sediment porosity variation patterns with time.

The variability results of sediment porosity indicate that the sediment porosity at a depth of 0.1 m ranged between 75.49% and 75.69%. Between 15 and 27 September, the porosity gradually decreased before abruptly increasing from 17 to 28 September. At a depth of 0.4 m, the porosity ranged from 69.63% to 73.49%. From 15 to 17 September, the porosity decreased rapidly before stabilizing until 27 September, and then abruptly decreased from 27 to 28 September. The sediment porosity at a depth of 0.6 m ranged between 74.31% and 74.78%, showing a gradual decrease from 15 to 28 September. At a depth of 0.9 m, the sediment porosity varied from 51.79% to 53.54%, and exhibited an overall increase of 3% from 15 to 27 September, followed by a gradual decrease from 27 to 28 September. The sediment porosity at a depth of 1.3 m remained essentially unchanged, ranging from 75.11% to 75.16% between 15 and 28 September. Finally, the sediment porosity at a depth of 1.6 m ranged between 69.24% and 69.45% and remained stable throughout the study period. These findings suggest that sediment porosity can vary significantly with depth and time and may provide valuable insights into sediment behavior and depositional processes in marine environments.

In this study, the sediment properties at various depths below the seafloor were investigated in order to better understand the behavior of sediment under pressure and over time. Specifically, the sediment porosity was monitored at depths of 0.1, 0.4, 0.6, 0.9, 1.3, and 1.6 m below the seafloor. The results showed that at depths of 0.1, 1.3, and 1.6 m below the seafloor, the sediment porosity remained stable and unchanged, indicating that the properties of the sediment in these layers did not change. However, at a depth of 0.4 m below the seafloor, the sediment porosity exhibited a trend of "decrease–increase–decrease" over time. At a depth of 0.6 m below the seafloor, the sediment porosity gradually increased over time, while at a depth of 0.9 m below the seafloor, the sediment porosity exhibited a clear increasing trend over time.

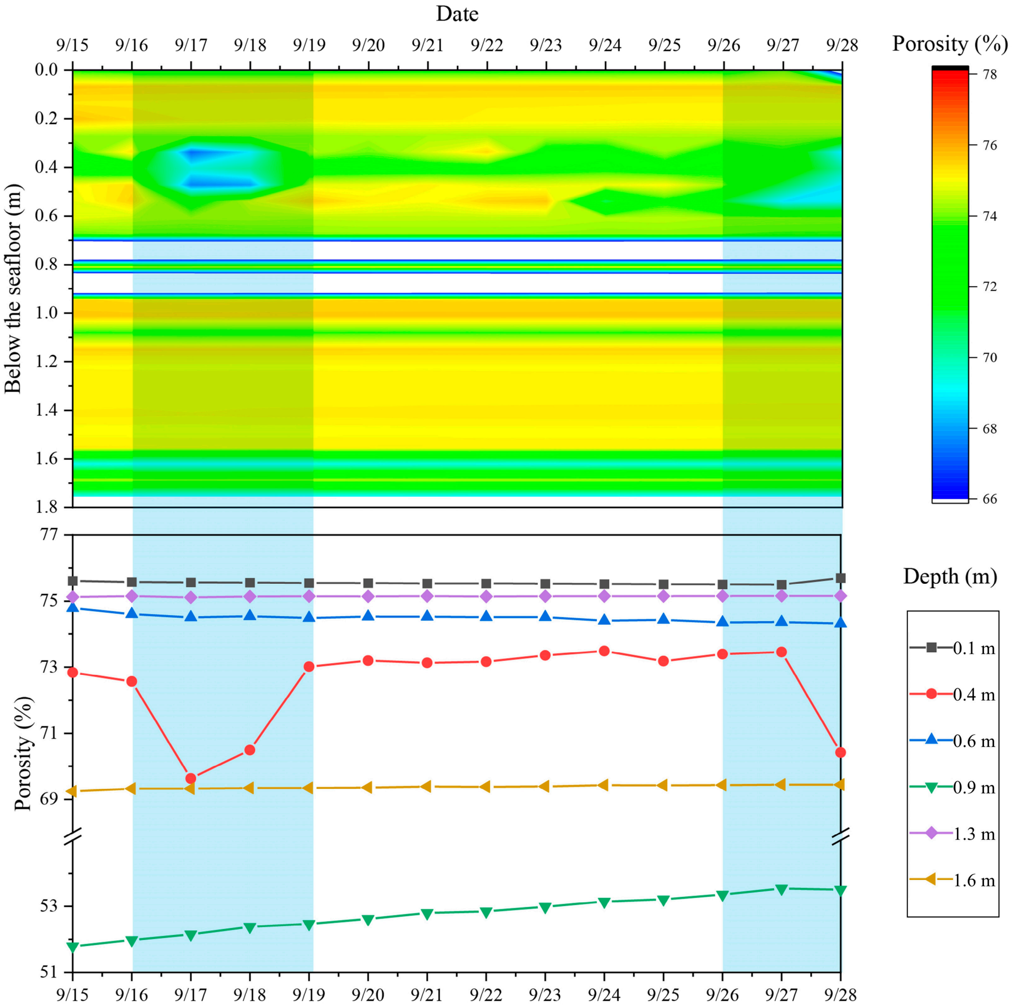

Figure 13. Temporal variation in porosity of the seafloor sediment in the South China Sea hydrate test area.

5. Conclusions

This study addresses the challenge of accurately inverting seafloor sediment physical properties and presents a model for the inversion of sediment physical properties based on a deep learning algorithm for seafloor sediment resistivity in offshore China. The deep learning algorithm establishes the relationship between seafloor sediment resistivity and key physical properties such as density, water content, and porosity in the hydrate test area of the South China Sea. This study clarifies the effect of the main controlling factors of density, water content, and porosity on resistivity and compares the differences between the deep learning inversion model and the empirical formula inversion model. The deep learning inversion algorithm is then used to invert the resistivity of seafloor sediments in the hydrate test area of the South China Sea, and the spatial distribution characteristics and dynamic changes in physical properties such as the density, water content, and porosity of the seafloor sediments are obtained. The results reveal the dynamic changes in sediment properties within 1.76 m below the seabed, providing valuable insights for future seafloor exploration and resource exploitation.

1. In this study, a novel model for the inversion of physical properties of seafloor sediments is presented. The model is based on a deep learning algorithm, which utilizes the TensorFlow and Keras deep learning databases to establish a six-layer neural network with a functional API. The mean squared error (MSE) is used as the loss function and the mean absolute error (MAE) is the supervisory function. The relationships between the resistivity of seafloor sediment and the density, water content, and porosity were established.

2. The use of seafloor sediment resistivity for the inversion of physical properties such as density, porosity, and water content has been explored. Empirical and deep learning relationships have been established, indicating that resistivity is strongly correlated with both porosity and water content in a power function, exhibiting a bipartite trend of "sharp decrease–slow decrease" with increasing water content. A good correlation between resistivity and density has also been identified, with density increasing in a "decrease–increase–sharp increase" three-stage trend as the resistivity increases.

3. The deep learning model exhibits a better fit and more accurate prediction capabilities than the empirical formula model. The empirical formula model is suitable for analyzing linear relationships with simple correlations and high correlation coefficients. In contrast, the deep learning inversion model is suitable for analyzing non-linear relationships with complex correlations and low correlation coefficients. When the model is trained with a large amount of data, the prediction results obtained using the deep learning inversion model are significantly better than those obtained using the empirical formula model. The deep learning inversion model improves the accuracy of the prediction range, resulting in a more concentrated prediction range and a higher prediction accuracy.

4. Based on in situ observations in the hydrate zone of the South China Sea, the physical properties of seafloor sediments in the hydrate zone of the South China Sea exhibit stratified variations. Specifically, in the range of 0–0.7 m below the seafloor, the density varies between 1.37 and 1.53 g/cm^3, the porosity varies between 73 and76%, and the water content varies between 122 and 124%. Within the 0.7–0.9 m depth range, the density varies between 1.43 and 1.60 g/cm^3, the porosity varies between 51 and 75%, and the water content varies between 43 and 124%. Lastly, in the range of 0.9–1.8 m, the density varies between 1.31 and 1.52 g/cm^3, the porosity varies between 69 and 76%, and the water content between 118 and 124%. These observations suggest that the physical properties of seafloor sediments in the hydrate zone exhibit distinct variations with depth, indicating the potential for stratified modeling of sediment properties in this region.

5. Based on long-term in situ observations in the hydrate zone of the South China Sea, the engineering properties of seafloor sediments in the region exhibit a four-layer feature that comprises low-resistivity, very high-resistivity, low-resistivity, and high-resistivity layers. Specifically, the resistivity of sediments at a depth of 0.3 m below the seafloor surface remains stable with time, while in the range of 0.3–0.7 m below the seafloor surface, the resistivity first increases and then decreases over time. In the range of 0.7–1 m below the seafloor surface, the resistivity decreases over time. At depths of 1–1.6 m below the seafloor surface, the resistivity remains stable over time, while at a depth of 1.6 m below the seafloor surface, the resistivity decreases over time. In addition, a layer containing hydrate is identified, displaying a resistivity bimodal structure with a value of 6.86 Ω·m.

6. By utilizing in situ resistivity observation data and a deep learning inversion sediment physical property model, the present study was able to identify a significant impact of hydrate decomposition on the sediment's physical properties. The observation period revealed that the resistivity increased in the range of 0–0.7 m below the seafloor, which coincided with a decrease in sediment density, water content, and porosity. Conversely, the resistivity decreased in the range of 0.7–0.9 m below the seafloor, which aligned with a decrease in sediment density and an increase in porosity and water content. In comparison to previous studies, this dynamic alteration was determined to be attributed to hydrate decomposition and the resultant gas production. It is hypothesized that the sediment dynamics at a depth of 0.7–0.9 m below the seafloor are instigated by the decomposition of

surface hydrate, whereas the sediment dynamics at a depth of 0–0.7 m below the seafloor are caused by the gas generated from hydrate decomposition.

Author Contributions: Conceptualization, Z.S. (Zhiwen Sun) and Y.J.; methodology, Z.F. and C.Z.; investigation, K.L.; resources, Z.S. (Zhongqiang Sun); writing—original draft preparation, Z.S. (Zhiwen Sun); writing—review and editing, X.S.; visualization, L.X. and H.L.; funding acquisition, Y.J. All authors have read and agreed to the published version of the manuscript.

Funding: This research was funded by the National Natural Science Foundation of China (nos. 41831280); the National Key R&D Program 2022YFC2803800; the National Natural Science Foundation of China (42207173, and 41427803, 42206078) , the Key R&D plan of Shandong Province 2022CXPT054 and Postdoctoral Applied Research Project of Qingdao (Assessment and Evaluation of the Carbon Sequestration Capacity of Jiaozhou Bay Salt Marshes).

Institutional Review Board Statement: Not applicable.

Informed Consent Statement: Not applicable.

Data Availability Statement: Available on request.

Acknowledgments: We acknowledge all experimenters, including Xiaomeng Li, Yue Qiao, Xianming Zhu, Na Zhu, Hong Zhang, Xiangqian Li, and Guan Yang, and all personnel of the Dongfanghong III and Marine Geology 6.

Conflicts of Interest: The authors declare no conflict of interest.

References

1. Gamboa, D.; Omira, R.; Terrinha, P. A Database of Submarine Landslides Offshore West and Southwest Iberia. *Sci. Data* **2021**, *8*, 185. [CrossRef]
2. Sun, Q.; Wang, Q.; Shi, F.; Alves, T.; Gao, S.; Xie, X.; Wu, S.; Li, J. Runup of Landslide-Generated Tsunamis Controlled by Paleogeography and Sea-Level Change. *Commun. Earth Environ.* **2022**, *3*, 244. [CrossRef]
3. Guo, X.; Stoesser, T.; Zheng, D.; Luo, Q.; Liu, X.; Nian, T. A Methodology to Predict the Run-out Distance of Submarine Landslides. *Comput. Geotech.* **2023**, *153*, 105073. [CrossRef]
4. Yin, S.; Pope, E.L.; Lin, L.; Ding, W.; Gao, J.; Wu, Z.; Yang, C.; Chen, J.; Li, J. Re-Channelization of Turbidity Currents in South China Sea Abyssal Plain Due to Seamounts and Ridges. *Mar. Geol.* **2021**, *440*, 106601. [CrossRef]
5. Zhu, C.; Li, S.; Chen, J.; Wang, D.; Song, X.; Li, Z.; Chen, B.; Shan, H.; Jia, Y. Nepheloid Layer Generation by Gas Eruption: Unexpected Experimental Results. *J. Ocean Limnol.* **2023**, *1*, 1–9. [CrossRef]
6. Jia, Y.; Zhang, L.; Zheng, J.; Liu, X.; Jeng, D.-S.; Shan, H. Effects of Wave-Induced Seabed Liquefaction on Sediment Re-Suspension in the Yellow River Delta. *Ocean Eng.* **2014**, *89*, 146–156. [CrossRef]
7. Guo, X.; Liu, Z.; Zheng, J.; Luo, Q.; Liu, X. Bearing Capacity Factors of T-Bar from Surficial to Stable Penetration into Deep-Sea Sediments. *Soil Dyn. Earthq. Eng.* **2023**, *165*, 107671. [CrossRef]
8. Bai, C.; Su, P.; Su, X.; Cui, H.; Shang, W.; Han, S.; Zhang, G. Characterization of the Sediments in a Gas Hydrate Reservoir in the Northern South China Sea: Implications for Gas Hydrate Accumulation. *Mar. Geol.* **2022**, *453*, 106912. [CrossRef]
9. Zhu, C.; Jiao, X.; Cheng, S.; Li, Q.; Liu, K.; Shan, H.; Li, C.; Jia, Y. Visualising Fluid Migration Due to Hydrate Dissociation: Implications for Submarine Slides. *Environ. Geotech.* **2020**, *40*, 1–9. [CrossRef]
10. Hui, Z. Study on the Reservoir Configuration of High Curvature Type Gravity Flow Channel in the Second Section of Yinggehai Formation, Dongfang Gas Field. Master Thesis, Northwestern University, Xi'an, China, 2021.
11. Vanneste, M.; Sultan, N.; Garziglia, S.; Forsberg, C.F.; L'Heureux, J.-S. Seafloor Instabilities and Sediment Deformation Processes: The Need for Integrated, Multi-Disciplinary Investigations. *Mar. Geol.* **2014**, *352*, 183–214. [CrossRef]
12. Guo, X.; Nian, T.; Fu, C.; Zheng, D. Numerical Investigation of the Landslide Cover Thickness Effect on the Drag Forces Acting on Submarine Pipelines. *J. Waterw. Port Coast. Ocean. Eng.* **2023**, *149*, 04022032. [CrossRef]
13. Zhou, S.; Li, Q. Developing ocean energy and building a strong ocean state. *Sci. Technol. Her.* **2020**, *38*, 17–26.
14. Sun, Z.; Jia, Y.; Shan, H.; Fan, Z.; Song, X.; Xue, L.; Li, K. Monitoring and Early Warning Technology of Hydrate-Induced Submarine Disasters. *IOP Conf. Ser. Earth Environ. Sci.* **2020**, *570*, 062030. [CrossRef]
15. Rezaei, S.; Shooshpasha, I.; Rezaei, H. Empirical Correlation between Geotechnical and Geophysical Parameters in a Landslide Zone (Case Study: Nargeschal Landslide). *Earth Sci. Res. J.* **2018**, *22*, 195–204. [CrossRef]
16. Zweiri, Y.H.; Whidborne, J.F.; Seneviratne, L.D. A Three-Term Backpropagation Algorithm. *Neurocomputing* **2003**, *50*, 305–318. [CrossRef]
17. Ciresan, D.C.; Meier, U.; Masci, J.; Gambardella, L.M.; Schmidhuber, J. Flexible, High Performance Convolutional Neural Networks for Image Classification. In Proceedings of the Twenty-Second International Joint Conference on Artificial Intelligence, Barcelona, Spain, 16–22 July 2011.

18. Ji, X.; Yang, B.; Tang, Q. Seabed Sediment Classification Using Multibeam Backscatter Data Based on the Selecting Optimal Random Forest Model. *Appl. Acoust.* **2020**, *167*, 107387. [CrossRef]
19. Singh, U.K.; Tiwari, R.K.; Singh, S.B.; Rajan, S. Prediction of Electrical Resistivity Structures Using Artificial Neural Networks. *J. Geol. Soc. India* **2006**, *67*, 234–242.
20. Luo, Z.F.; Lu, B.; Yang, Y. Application of artificial neural network technology to submarine sediment sound velocity prediction. *Mar. Technol.* **2009**, *28*, 40–43.
21. Mukherjee, B.; Sain, K. Prediction of Reservoir Parameters in Gas Hydrate Sediments Using Artificial Intelligence (AI): A Case Study in Krishna-Godavari Basin (NGHP Exp-02). *J. Earth Syst. Sci.* **2019**, *128*, 199. [CrossRef]
22. Zhou, Y.; Wang, J.; Zuo, R.; Xiao, F.; Shen, W.; Wang, S. Machine learning, deep learning and Python language in field of geology. *ACTA Petrol. Sin.* **2018**, *34*, 3173–3178.
23. Singh, H.; Seol, Y.; Myshakin, E.M. Prediction of Gas Hydrate Saturation Using Machine Learning and Optimal Set of Well-Logs. *Comput. Geosci.* **2021**, *25*, 267–283. [CrossRef]
24. Chen, J.; Vissinga, M.; Shen, Y.; Hu, S.; Beal, E.; Newlin, J. Machine Learning-Based Digital Integration of Geotechnical and Ultrahigh-Frequency Geophysical Data for Offshore Site Characterizations. *J. Geotech. Geoenvironmental Eng.* **2021**, *147*, 04021160. [CrossRef]
25. Singh, A.; Ojha, M. Machine Learning in the Classification of Lithology Using Downhole NMR Data of the NGHP-02 Expedition in the Krishna-Godavari Offshore Basin, India. *Mar. Pet. Geol.* **2022**, *135*, 105443. [CrossRef]
26. Pszonka, J.; Schulz, B. SEM Automated Mineralogy Applied for the Quantification of Mineral and Textural Sorting in Submarine Sediment Gravity Flows. *Gospod. Surowcami Miner. Miner. Resour. Manag.* **2022**, *38*, 105–131.
27. Xie, Y.; Lu, J.; Cai, H.; Deng, W.; Kuang, Z.; Wang, T.; Kang, D.; Zhu, C. The In-Situ NMR Evidence of Gas Hydrate Forming in Micro-Pores in the Shenhu Area, South China Sea. *Energy Rep.* **2022**, *8*, 2936–2946. [CrossRef]
28. Yang, Y.; Kou, H.; Li, Z.; Jia, Y.; Zhu, C. Normalized Stress–Strain Behavior of Deep-Sea Soft Soils in the Northern South China Sea. *J. Mar. Sci. Eng.* **2022**, *10*, 1142. [CrossRef]
29. Guo, X.-J.; Zhang, Z.-K.; Jia, Y.-G.; Huang, X.-Y. Electrical resistivity feature of saturated silty soil in Yellow River estuarine area and its engineering geology application. *J. Rock Soil Mech.* **2007**, *28*, 593–598.
30. Li, D.; Ye, Y.; Chen, P.; Chen, X.; Lv, X. Shelf Sediment Resistivity Property off Ningbo Coast. *Geotech. Investig. Surv.* **2010**, *38*, 19–22.
31. Yu, L. Relationship between Resistivity and Mechanical Properties of Shallow Soil in Gas Hydrate Mining Area of South China Sea. Master Thesis, Ocean University of China, Qingdao, China, 2019.
32. Nguyen, Q.V.; Miller, N.; Arness, D.; Huang, W.; Huang, M.L.; Simoff, S. Evaluation on Interactive Visualization Data with Scatterplots. *Vis. Inform.* **2020**, *4*, 1–10. [CrossRef]
33. Viau, C.; McGuffin, M.J.; Chiricota, Y.; Jurisica, I. The FlowVizMenu and Parallel Scatterplot Matrix: Hybrid Multidimensional Visualizations for Network Exploration. *IEEE Trans. Vis. Comput. Graph.* **2010**, *16*, 1100–1108. [CrossRef]
34. Wu, C.L.; Chau, K.W.; Fan, C. Prediction of Rainfall Time Series Using Modular Artificial Neural Networks Coupled with Data-Preprocessing Techniques. *J. Hydrol.* **2010**, *389*, 146–167. [CrossRef]
35. Grattarola, D.; Alippi, C. Graph Neural Networks in TensorFlow and Keras with Spektral [Application Notes]. *IEEE Comput. Intell. Mag.* **2021**, *16*, 99–106. [CrossRef]
36. Khan, M.A.; Zafar, A.; Farooq, F.; Javed, M.F.; Alyousef, R.; Alabduljabbar, H.; Khan, M.I. Geopolymer Concrete Compressive Strength via Artificial Neural Network, Adaptive Neuro Fuzzy Interface System, and Gene Expression Programming With K-Fold Cross Validation. *Front. Mater.* **2021**, *8*, 621163. [CrossRef]
37. Kim, T.; Oh, J.; Kim, N.; Cho, S.; Yun, S.-Y. Comparing Kullback-Leibler Divergence and Mean Squared Error Loss in Knowledge Distillation. *arXiv* **2015**, arXiv:2105.08919.
38. Sun, Z.; Jia, Y.; Quan, Y.; Guo, X.; Liu, T.; Meng, Q.; Sun, Z.; Li, K.; Fan, Z.; Chen, T.; et al. Development and Application of Long-Term in Situ Monitoring System for Complex Deep-Sea Engineering Geology. *Earth Sci. Front.* **2022**, *29*, 216–228. [CrossRef]
39. Hamilton, E.L.; Bachman, R.T. Sound Velocity and Related Properties of Marine Sediments. *J. Acoust. Soc. Am.* **1982**, *72*, 14. [CrossRef]
40. Sun, Y.F.; Sun, H.F.; Dong, L.F. Resistivity characteristics of submarine soils and their corrosion evaluation. *Coast. Eng.* **2005**, *14*, 48–53.
41. Liu, G.H.; Wang, Z.Y.; Huang, J.P. Resistivity properties of soils and their engineering applications. *J. Geotech. Eng.* **2004**, *1*, 83–87.
42. Archie, G.E. The Electrical Resistivity Log as an Aid in Determining Some Reservoir Characteristics. *Trans. AIME* **1942**, *146*, 54–62. [CrossRef]
43. Jana, S.; Ojha, M.; Sain, K.; Srivastava, S. An Approach to Estimate Gas Hydrate Saturation from 3-D Heterogeneous Resistivity Model: A Study from Krishna-Godavari Basin, Eastern Indian Offshore. *Mar. Petrol. Geol.* **2017**, *79*, 99–107. [CrossRef]
44. Wu, J.; Guo, X.; Jia, Y.G.; Sun, X.; Li, N. Simulation and analysis of the monitoring effect of sea-bed based high-density resistivity method for methane gas leakage during natural gas hydrate extraction. *J. Jilin Univ. (Earth Sci. Ed.)* **2018**, *48*, 1854–1864.
45. Cong, J.; Zhang, Y.; Hu, G.; Mi, B.; Kong, X.; Xue, B.; Ning, Z.; Yuan, Z. Textures, Provenances, and Transport Patterns of Sediment on the Inner Shelf of the East China Sea. *Cont. Shelf Res.* **2022**, *232*, 104624. [CrossRef]
46. Feng, M. Numerical Simulation of Hydrate Particle Migration and Deposition in Horizontal Pipe Flow. *Value Eng.* **2023**, *42*, 148–150.
47. Du, X.; Sun, Y.; Song, Y.; Zhu, C. In-situ observation of wave-induced pore water pressure in seabed silt in the yellow river estuary of China. *J. Mar. Environ. Eng.* **2021**, *10*, 305–317.